Journal Pre-proof

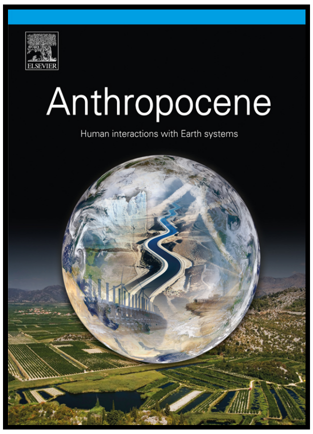

Spatial patterns of soil salinity in the central Argentinean Dry Chaco

Michiel Maertens, Gabriëlle J.M. De Lannoy, Frederike Vincent, Samuel Massart, Raul Giménez, Javier Houspanossian, Ignacio Gasparri, Veerle Vanacker

PII: S2213-3054(22)00003-0
DOI: https://doi.org/10.1016/j.ancene.2022.100322
Reference: ANCENE100322

To appear in: *Anthropocene*

Received date: 8 June 2021
Revised date: 15 January 2022
Accepted date: 18 January 2022

Please cite this article as: Michiel Maertens, Gabriëlle J.M. De Lannoy, Frederike Vincent, Samuel Massart, Raul Giménez, Javier Houspanossian, Ignacio Gasparri and Veerle Vanacker, Spatial patterns of soil salinity in the central Argentinean Dry Chaco, *Anthropocene*, (2021) doi:https://doi.org/10.1016/j.ancene.2022.100322

Spatial patterns of soil salinity in the central Argentinean Dry Chaco

Michiel Maertens[1,2], Gabriëlle J.M. De Lannoy[2], Frederike Vincent[2], Samuel Massart[2,3], Raul Giménez[4], Javier Houspanossian[4], Ignacio Gasparri[5],Veerle Vanacker[1]

[1] Earth and Life Institute, George Lemaître Center for Earth and Climate Research, Université Catholique de Louvain, L4.03.08, Louvain-la-Neuve, 1348, Belgium

[2] Department of Earth and Environmental Sciences, KU Leuven, Belgium

[3] Department of Geodesy and Geoinformation, TU Wien, Austria

[4] Grupo de Estudios Ambientales, Universidad Nacional de San Luis, Argentina

[5] Institute of Regional Ecology, CONICET, National University of Tucumán, Argentina

Corresponding Authors:

Michiel Maertens (michiel.maertens@vito.be),
Veerle Vanacker(veerle.vanacker@uclouvain.be)

Acknowledgements

This research was performed with support from the Belspo project REFORCHA (SR/00/338) and C1 KU Leuven (C14/16/045). The computer resources and services used in this work were provided by the Flemish Supercomputer Center (VSC), funded by the Research Foundation - Flanders (FWO) and the Flemish Government. The authors thank Martin Requena for his support during the field campaign, and Marco Bravin (UCLouvain) for technical assistance with the calibration of the field sensors.

Abstract

The Dry Chaco is a semi-arid ecoregion in South America that hosts one of the largest dry forests in the world, but expansion of dryland agriculture and cattle ranching led to gradual conversion of native vegetation to anthropogenic land cover. The potential impact of these newly established agricultural lands on the surrounding environment is of great concern. Local studies have shown that deforestation leads to changes in the soil-water balance, and can expedite groundwater rise and mobilization of water-soluble salts to the surface affecting plant growth and crop productivity. This study is a regional assessment of soil salinity and salinization processes in the central Argentinean Dry Chaco. It is based on extensive dataset of 492 surface and 142 subsurface samples taken along east-west transects across the Dry Chaco. Soil electrical conductivity (EC) was used as an indicator of salinity, and supplementary information on salt crusts was derived from Google Earth imagery. Subsurface salinity (i.e., measured at 100 cm depth) showed clear regional patterns in natural soil salinity that are related to the annual water budget and topography. Besides primary salinization due to arrested drainage and landscape stagnation, anthropogenic activities increased secondary salinization, especially in the agricultural areas with shallow groundwater tables and irrigated croplands. In addition, the study demonstrated that remotely-sensed vegetation indices such as the seasonal variation in the density of green vegetation are particularly suitable to monitor regional variation in soil salinity. Our results show that the extent of future dryland salinization in the Dry Chaco will mainly depend on whether areas prone to natural soil salinity are further protected from deforestation, and the magnitude and rate of groundwater rise after deforestation as conditioned by local climate and geomorphology. This better understanding of soil salinity patterns and how they are affected as a result of anthropogenic activities is important for the implementation of appropriate and effective measures to prevent severe salinization.

Keywords

Salinization, Subtropical woodlands, Deforestation, Soil degradation, Electrical conductivity

1 Introduction

Soil salinization is the process whereby water-soluble salts accumulate in the soil mantle. Salinization degrades the soil when the concentration of salts rises above a level that impacts agricultural production or threatens ecosystems (Rengasamy, 2006). A soil is defined as saline when the electrical conductivity (EC) of the saturation extract in the root zone exceeds 4 dS/m, a level at which most crops experience reduced yield due to root osmotic stress, ion-toxicity, and anoxia (Richards, 1954, Walker et al., 1999; Turnbull et al., 2012). On a global scale, salinization is one of the major soil degradation threats and affects an area of approximately 8,322,000 km^2 (6% of the world's total land area) (Munns, 2005; Rengasamy, 2006). Multiple processes are involved in the development of saline soils, whereby a distinction can be made between natural (so-called primary) and human-induced (secondary) salinity (Daliakopoulos et al, 2016).

Natural salinity is determined by how chemical weathering processes release salts from the parent material, resultant from the mineralogy of rock or sediment constituents (Daliakopoulos et al., 2016), and how salts are distributed in the landscape. The redistribution of these salts within the soil mantle is controlled by the regional climate, hydrogeology and vegetation cover. The annual climatic water balance, here represented by precipitation minus potential evapotranspiration (*P-Pet*) strongly influences salinization (Nosetto et al., 2008). A positive water balance results in a net downward water flux and low salinity, whereas a negative water balance leads to evapotranspiration deficits that can be offset by groundwater rise. This can cause a net upward flux of groundwater and solutes towards the surface and enhance salt accumulation in the soil mantle (Schofield et al., 2001; Nosetto et al., 2008). Specific hydrogeological circumstances, such as the depth of the groundwater table may further amplify or weaken the hazard (Domenico and Schwartz, 1998).

Besides natural contributing factors, anthropogenic activities can influence soil salinity (Nosetto et al., 2008). Human-induced vegetation changes can alter the local water balance through changes in transpiration rates (Peña-Angulo et al., 2021) and induce severe soil salinization as experienced in Western Australia (Lambers, 2003). Furthermore, irrigation with saline water and poorly managed irrigation schemes (often coupled with poor drainage conditions) are an important source of secondary salinization and major factor limiting crop production (Fan et al., 2012; Trnka et al., 2013).

Mapping and monitoring soil salinity is important for sustainable management of drylands (Scudiero et al., 2014b). A plethora of studies and methods exist to map soil salinity based on remote sensing data (e.g., Metternicht and Zinck (2003); Zhang et al. (2011); Scudiero et al. (2015); Zhang et al. (2015)). Vegetation indices are frequently used as indirect measures of soil salinity (Metternicht and Zinck, 2003; Zhang et al., 2011), as excessive salt concentrations affect vegetation growth. Most studies derived vegetation indices from yearly to multi-year spectral data (Lobell et al., 2010; Wu et al., 2014; Zhang et al., 2015; Scudiero et al., 2014a, 2015), or integrated values over the growing season (Zhang et al., 2015). However, studies were usually conducted at a local scale and the locally developed algorithms are not fully extendable for regional-scale assessments due to spatial variability in climate conditions, soil properties, and land use/management (Wu et al., 2014). Besides, a major problem with indirect salinity detection methods is that remotely sensed vegetation indices generally cannot differentiate salinity-induced crop stress from stress caused by other factors such as weather conditions, pests, and water management (Vanacker et al., 2005, Hopmans et al., 2021). Furby et al. (2010) showed that environmental covariates can improve the accuracy of salinity maps when they are used as additional predictor variables in regression equations and classifiers. Case-studies on soil salinity assessments for California (Scudiero et al. 2015) and Iran (Taghizadeh-Mehrjardi et al.

2021) included data on precipitation, temperature and topography and multitemporal Landsat 7 canopy reflectance data.

A region that is characterized by primary and secondary salinity is the Dry Chaco in South America. The Dry Chaco covers one of the most extensive and flat sedimentary plains in the world including parts of Argentina, Paraguay and Bolivia (787,000 km^2). This low-relief region is prone to salinization because of its subhumid to semi-arid climate (Jobbágy et al., 2020). The Dry Chaco still hosts large remnants of dry forests (Marchesini et al., 2017), but has long been one of the largest deforestation hotspots in the world (Hansen et al., 2013). Large-scale land cover change in the Chaco affects local hydrology and may introduce dryland salinity. Native dry forests in the Chaco consume water intensively, preventing deep drainage of rain water to the groundwater table (Amdan et al., 2013; Jobbágy et al., 2020). As a result, salts remain or accumulate in the soil mantle (Giménez et al., 2020b). When forests are converted to agricultural land, soil moisture and deep drainage increase, resulting in a rise in the groundwater table. If this trend continues over time, it may result in salt accumulation close to the soil surface and eventually result in reduced plant growth and soil degradation (Giménez et al., 2016; Marchesini et al., 2017; Jobbágy et al., 2020).

The above-mentioned studies from the Dry Chaco are mostly conducted on plot-level scale and relate soil salinization to forest conversion. To our knowledge, no studies exist on the regional pattern of primary and secondary soil salinity over the Dry Chaco or on how environmental conditions such as topography and climate influence this pattern. Hence, this study is guided by the following research questions: (i) Which environmental variables are associated with the observed regional salinity patterns over the Dry Chaco? (ii) Which remote-sensed vegetation indices are relevant predictors of regional salinity? (iii) Which processes explain the observed geographic distribution of salinity? To answer these questions, we collected 492 surface and 142 subsurface soil electrical conductivity (EC) measurements along east-west transects covering the existing topographic and climatic gradients of the region.

2 Methodology

2.1 Study area

The Dry Chaco is a sedimentary plain located at the transition between the Subandean Ranges and the adjacent lowlands (Latrubesse et al., 2012). Its elevation ranges from ca. 600 m in the west towards 40 m in the east (Figure 1a). The area is drained by 5 principal rivers that have their headwaters in the Subandean Ranges (Moretti et al., 2019), and have formed megafans that extend 500 to 700 km from the Andean foothills (Thalmeier et al., 2021). The Dry Chaco ecoregion has a north-south gradient in annual mean temperature from 26°C to 18°C (Minetti et al., 1999). The annual mean precipitation ranges from 400 mm/year in the central part to 1000 mm/year in the eastern and western parts (Minetti et al., 1999). Most precipitation falls during the wet season, which lasts from October till March. Soils in the Chaco mainly developed on fluvial sediments, and to a lesser extent on lacustrine and aeolian parent material. The fluvial sediments are sandy in the alluvial (paleo-)channels and more clayey in the floodplains, whereas the aeolian sediments are silty and referred to as loess (Moretti et al., 2019). This study focuses on the central part of the Argentinean Dry Chaco (Figure 1b).

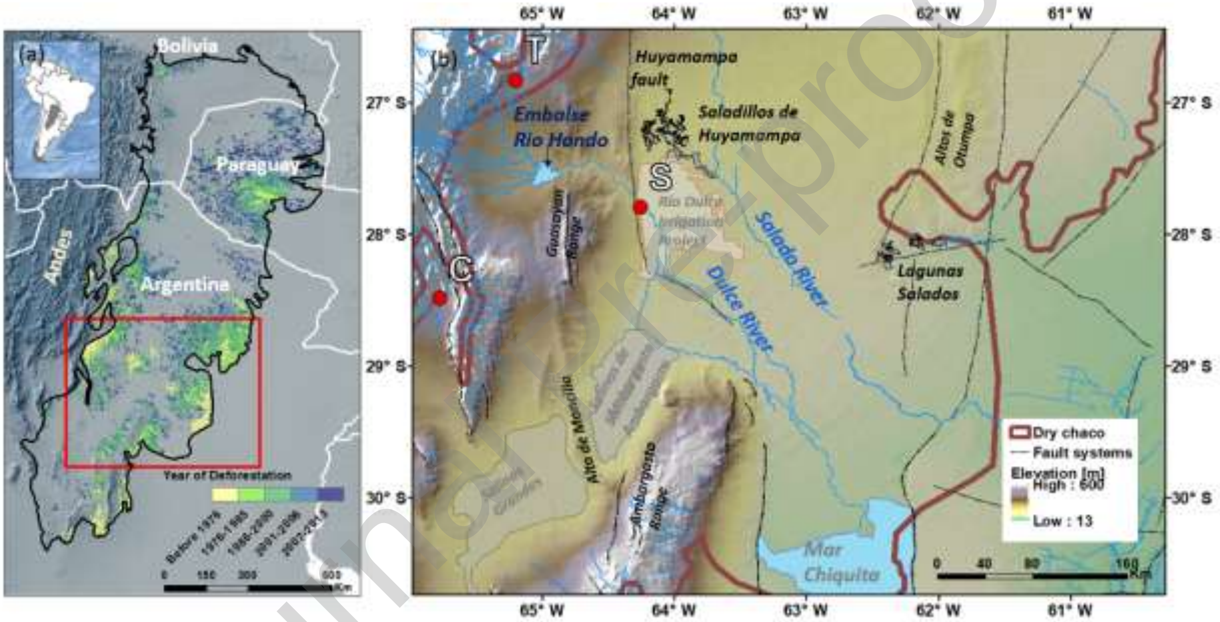

Figure 1: (a) Geographic location of the Dry Chaco in South America, with spatio-temporal pattern of deforestation between 1976 and 2013 as derived from Vallejos et al. (2015). (b) Topography and main geomorphological features of the central Argentinean Dry Chaco. The largest cities are (T) San Miguel de Tucumán, (S) Santiago Del Estero and (C) Catamarca.

Tectonic deformation in the region has been active throughout the Quaternary and mainly includes east-west compression (Mon and Gutiérrez, 2009; Gutiérrez et al., 2017). The fault scarp of the 60 km long Huyamampa thrust Fault is a result of this compression and is clearly visible in the landscape with an offset of approximately 150 to 200 m (Miro and Gonfiantini, 1980). The adjacent salt lakes, Saladillos de Huyamampa, are likely formed as a result of water accumulation (water seepage and blocked drainage) in the fault-bounded depression. Near Santiago del Estero, the Huyamampa Fault forms the border of the alluvial deposits of the Dulce river. This alluvial megafan has a thickness of about 150 m at its apex and it thins eastward over a distance of 50 km (Bhattacharya et al., 2006). Quaternary tectonic activity in the northeastern part of the study area initiated the progressive uplift of the Altos de Otumpa Range, a topographic high with north-south orientation (Peri, 2012). In the topographic depression that formed south of the Altos de Otumpa, a series of small salt lakes developed, the Lagunas Saladas (Peri, 2012). In the southern Dry Chaco, Quaternary east-northeast transtension resulted in the formation of a large topographic depression. Together with the uplift of the Alto de Mancilla Range, and diversion of the Dulce/Sali River , two saline paleo-lakes (Salinas Grandes and Salinas de Ambargasta) are formed (Figueroa et al., 2020).

In the Dry Chaco, the natural vegetation pattern is a patchwork of seasonally dry and xerophytic forests to halophytic shrublands and herbaceous plants in saline-affected areas (Gobbi et al., 2020). The area underwent rapid land cover change in the last decades (Vallejos et al., 2015). Commercial forest exploitation and related deforestation activities started at the beginning of 20th century, with selective logging of Quebracho Colorado (*Schinopsis quebracho colorado*), a tree species with very dense wood that is used for railroad sleepers and tannin extraction (Bucher and Huszar, 1999; Rueda et al., 2015). Since the 1970s, the deforestation rate accelerated quickly: global food demand started to rise and technological improvements together with favorable climatic conditions made a large part of the Dry Chaco suitable for agriculture (Marchesini et al., 2017). Since 1976, more than 158,000 km^2 of forest was transformed into agricultural land (Figure 1a), mainly for soybean production, corresponding with a loss of about 20.7% of the original dry forest (Vallejos et al., 2015; De Marzo et al., 2021). Near Santiago del Estero, numerous small-sized farms intensively use the Rio Dulce alluvial cone for irrigated agriculture (Figure 1b). With an irrigable area of 1,200 km^2, it is one of the most important irrigation systems in Argentina (Prieto, 2006) fed by the Rio Hondo Reservoir.

2.2 Data collection

Data on soil salinity was collected during a two-month field campaign in July-August 2019 across the central part of the Argentinean Chaco (Figure 2). Samples were collected along multiple east-west transects through the provinces of San Miguel de Tucumán, Santiago del Estero and Chaco. The exact location of the transects was conditioned by road accessibility. To avoid direct influence of the road, all samples were taken at > 50 m from the road. As a proxy for soil salinity, we measured the EC of 50 grams of soil taken at 5 cm and 1 m depth. The 1:1 method was used, whereby 50 ml of distilled water was added to 50 grams of soil. The samples were shaken and left to rest for 15 minutes, after which the temperature corrected EC (expressed in dS/m) was measured with a YSI proDSS probe. The YSI proDSS EC sensor measures EC values in a range from 0 to 200 dS/m with an accuracy of 0.001 dS/m. The sensor was calibrated daily. The dataset contains 492 surface and 142 subsurface measurements resulting in one subsurface measurement per km^2. Despite the low number of subsurface samples, maximum coverage of topographic and climatic conditions was ensured by comparing the spatial distribution of multiple environmental variables over the entire study area with the one of the sampling points (Appendix A.2).

During the field campaign, soil salt crusts at the surface were observed. In agriculture land, the crusts were small (<2 m in diameter), patchy and with irregular shapes. In topographic depressions however, they covered extensive areas (>1 km^2). After the field campaign, available Google Earth imagery (2013-2019) was used to locate clusters where salt crusts were present. The inspection was based on differences in surface reflectance between salt and non-salt affected surfaces (Appendix A.1). Figures 2a-d illustrate how salt crusts encountered during the field campaign appear in Google Earth imagery.

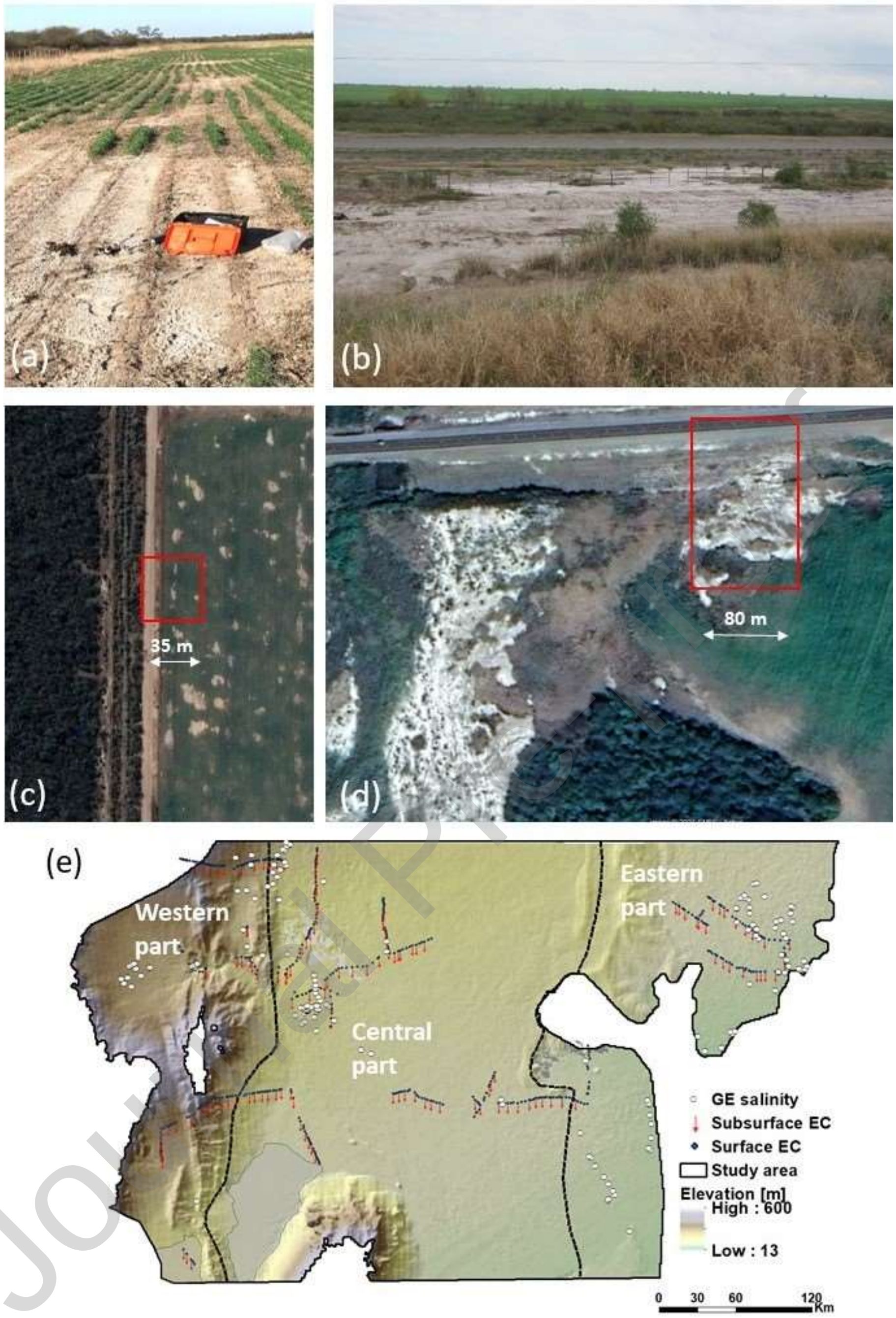

Figure 2: (a-b) Signs of surface salinity observed during the field campaign (a: 26°42'50" S, 64°16'20" W, b: 26°40'40" S, 64°28'10" W) and (c-d) how they appear on Google Earth imagery. (e) Location of soil samples collected during the field campaign of 2019, with indication of surface (blue dot) and subsurface (red arrow) samples. White dots correspond to the areas where signs of surface salinity were detected based on Google Earth imagery. The north-south black dotted lines mark the division into geomorphological units.

The spatial domain of the study was determined by the upper and lower latitude of the sampling dataset, and the limits of the Dry Chaco ecosystem. Areas above > 500 m a.s.l. were excluded. The results are discussed for three geomorphological units : (i) a western part, including the areas west of the Huyamampa Fault and the Alto de Mancilla, (ii) a central part corresponding with the flat lowlands of the Chaco plain, and (iii) an eastern part with the areas east of the Altos de Otumpa and related fault systems (Figure 2e).

2.3 Environmental variables

To gain more insights in the spatial pattern of soil salinity, the EC values were associated to topography, satellite-derived Leaf Area Index (*LAI*) and Greenness Vegetation Fraction (*GVF*), climatic water balance (represented as *P-Pet*), and soil moisture (*SM*) as potentially relevant variables. For *P-Pet*, *SM* and vegetation, the mean and standard deviation over the previous hydrological year (September 2018-2019) was used. Variables that showed a significant correlation with the point-scale EC measurements were included in the regression analysis.

2.3.1 Topographic data

Topographic information was derived from the Multi-Error-Removed Improved-Terrain Digital Elevation Model (MERIT DEM) (Yamazaki et al., 2019), representing the terrain elevations at 3 arcsec resolution (~90 m at the equator). As local depressions, where groundwater is close to the surface, are hypothesized to be more prone to salinization, the DEM was detrended to better represent local topography. To do so, first, we created a surface by interpolating the altitude of the lowest points in the landscape (river channels, lakes). Second, the interpolated surface was substracted from the original DEM. In the detrended DEM, topographic depressions obtained the lowest absolute elevation values. We will further refer to this detrended DEM as $DEM_{detrend}$. The DEM was upscaled to 1 km to match the resolution of the hydrological data.

2.3.2 Vegetation data

Two satellite-derived vegetation indices were derived as indirect indicators of soil salinity: the Leaf Area Index (*LAI*) and the Greenness Vegetation Fraction (*GVF*). The *LAI* characterizes plant canopies, and expresses the leaf area per unit ground area (Smets et al., 2016). Satellite-derived *LAI* values correspond to the total green *LAI* of all canopy layers, including the understory which may be significant in forests. The *GVF* corresponds to the fraction of ground covered by green vegetation. It is computed from the *LAI* and other canopy structural variables. The *GVF* and *LAI* data used in this study are obtained from the Copernicus Global Land Service. The datasets have a resolution of 300 m and spatially complete maps are available every 14 days from January 2009 onwards. From 2014 onwards, the indices were derived from Top of Atmosphere PROBA-V reflectances in three visual-near infrared spectral bands allowing to distinguish healthy from unhealthy vegetation (Smets et al., 2016). To match the resolution of the hydrological data, *LAI* and *GVF* values were upscaled by spatial averaging.

2.3.3 Precipitation, evapotranspiration and soil moisture data

Spatio-temporal information on soil moisture (*SM*) was obtained from NOAH LSM version 3.6 (Ek et al., 2003), embedded in the NASA Land Information System (Kumar et al., 2008). NOAH produces daily fluxes and states of the surface water and energy budget. A spatial resolution of 1 km was used for the simulations and aggregated on a daily basis using a model integration timestep of 15 min. The meteorological forcing data (precipitation, air temperature, specific humidity, radiation, wind and surface pressure) were extracted from the Modern-Era Retrospective analysis for Research and Applications (MERRA-2) product (Gelaro et al., 2017) with inclusion of gauge-based precipitation corrections (Reichle et al., 2017). To represent vegetation density, the satellite-derived *LAI* and *GVF* were used as described in section 2.3.2. Soil texture in the LSM was defined as loamy sand for the entire study area, which is a simplification of soil data from Moretti et al. (2019). The implementation of detailed soil data did not necessarily improve the correlation between modelled and in-situ soil moisture (Massart, 2020). The LSM was run with yearly updated land cover information derived from the European Space Agency-Climate Change Initiative (ESA-CCI) land cover product (Kirches et al., 2014). The time-varying vegetation and land cover data allow for an up-to-date and accurate description of the land surface (Maertens et al., 2021). The LSM was spun up for 7.5 years from 1 January 2011 through 31 August 2018. The simulations covering the period 01/09/2018 till 31/08/2019 were used for further analysis.

Pet is here defined as the reference crop evapotranspiration and was calculated using the Food and Agriculture Organization (FAO) Penman-Monteith method (Allen et al., 1998). The necessary climate data (temperature, windspeed, atmospheric pressure and solar radiation) for the calculations were derived from the MERRA-2 product (Gelaro et al., 2017), bilinearly interpolated to 1 km resolution. The annual water balance was calculated by subtracting the annual *Pet* from the annual *P* derived from MERRA-2 (also downscaled to a 1 km resolution). Negative values result in a water deficit, whereas positive values indicate water excess. We did not use the ratio of *Pet/P*, as very low *P* values during the dry months caused unrealistic *Pet/P* ratios when calculating monthly means (see section 2.3.4).

2.3.4 Assumptions about temporal variability

Soil salinity - just as other physico-chemical soil properties - varies over time. Temporal variation typically occurs at different timescales ranging from multi-annual over inter-annual or seasonal variation (Pennington and Chavez, 2000; Nosetto et al., 2013) to event-based variation (Glatzle et al., 2020). The multi-annual or first-order variation is associated with cyclical changes in climate (Gutierrez and Johnson, 2010) or land cover change (Jobbágy et al., 2020). Inter-annual hydrometeorological variability such as extreme wet years can generate second-order variation in soil salinity. Individual hydrometeorological events (such as significant precipitation events, after which salts are diluted or leached by rainwater infiltration) generate third-order temporal variations in soil salinity. However, by design, most soil salinity maps are static in time, focus on spatial variations and make abstractions of temporal variations in salinity.

In this study, the EC measurements were collected in July-August 2019. As such, the large-scale salinity map will closely mimic the soil salinity as it was observed in the dry season of 2019 and might not be fully representative for long-term annual mean salinity patterns. Given the wide spread in EC values measured across the study area we assume that the inter-annual variations at a given location are small compared to the spatial variations in EC over the study area. The EC measurements were associated with simulations on soil moisture, the climatic water balance and vegetation from the previous hydrological year (01/09/2018 till 31/08/2019). It is important to mention that the eastern part of the study area had an anomalous wet period (May-June 2019) prior to the field campaign, possibly resulting in salt dilution. Besides average annual hydrometeorological data, seasonal variation was taken into account by the use of an annual standard deviation map for each variable. This was done by first calculating monthly mean maps for each variable for the period September 2018-2019, and then deriving the standard deviation over the 12 months of data for each pixel. The standard deviation maps allow to distinguish areas with low and high seasonality, and they can identify potential bias related to cropping cycles. For example, agriculture plots that are fallow for part of the year can incorrectly be interpreted as saline areas if only the annual mean vegetation *GVF* or *LAI* is included. The use of standard deviations maps (further referred to as σ_{variable}) allows to overcome this issue as they incorporate the effect of seasonal vegetation cycles. In summary, the 1-year means and standard deviations of 4 variables and a detrended DEM (nine variables in total) at 1-km resolution are used as predictor variables in the regression analyses: *P-Pet*, $\sigma_{P\text{-}Pet}$, *GVF* , σ_{GVF} , *LAI*, σ_{LAI}, *SM*, σ_{SM} and $DEM_{detrend}$.

2.4 Selection of relevant variables and regression analysis

Prior to the analysis, the nine variables were standardized using a spatial Z-score transformation: for each pixel, the spatial mean was subtracted from the original value, and the difference was divided by the spatial standard deviation. Their correspondence with soil salinity was quantified using Spearman correlation analysis (R_{SP}). The variables were tested on multicollinearity: the variable inflation factor (VIF) was calculated and variables with a VIF > 3 were omitted in the final regression model. Variables with a $R_{SP} \geq 0.40$ and P value ≤ 0.05 were considered as significant variables and selected as input in the regression model.

The Multivariate Adaptive Regression Splines (MARS) technique, developed by Friedman (1991), was used to relate EC values to the environmental variables. The advantage of this technique is that it allows to account for the non-linear and non-parametric relation between variables. The building elements in the MARS model are piece-wise spline functions. These functions divide the data range into separate piece-wise linear or cubic segments, called splines (Rounaghi et al., 2015; Kisi and Parmar, 2016; Roy et al., 2018; Adnan et al., 2020). The ARESLab toolbox for Matlab was used for the MARS regression (Jekabsons, 2016).

The final salinity map is the result of a cross-validation approach. A total of 100 model simulations were conducted whereby for each iteration, 4/5 of the EC measurements was randomly selected for model calibration and 1/5 for internal model validation. By calculating the ensemble-mean over the 100 simulations, the mean salinity over the dry season was obtained. The standard deviation on the mean is an indicator of the uncertainty on the modelled salinity values. Since the random cross-validation does not ensure independent sampling, the ensemble uncertainty will underestimate the actual prediction uncertainty (Roberts et al., 2017). The model output was evaluated against the measured EC-values by means of the coefficient of determination (R^2) and Root Mean Square Error (RMSE).

3 Results

3.1 Spatial variability in observed surface and subsurface salinity

The geographic distribution of surface and subsurface soil EC values and salt crusts is shown in Figure 3. Generally, the western part is characterized by low surface EC values (majority of the values ranges between 0 and 2 dS/m), although extremely high values occur near the Salinas Grandes (> 40 dS/m) in the South. In the central part, the mean surface EC values are higher but show higher spatial variability (mean of 4.3 dS/m ± 7.7 dS/m). The highest EC values are found over the Salinas de Ambargasta and the Saladilos de Huyamampa. Observed surface EC values over the eastern part are generally low (0.58 ± 1.46 dS/m). Agricultural fields with salinization were identified on Google Earth imagery west of the Rio Hondo Reservoir, near the Huyamampa Fault at the transition from the western to the central part and on the irrigated croplands of the Rio Dulce Irrigation project. Despite the fact that low EC values were measured during the field sampling, numerous salt crusts were identified over the lowest areas of the eastern part. This is likely a result of the seasonal character of surface salinity in this part of the Chaco.

The subsurface measurements show large-scale patterns that are similar to the surface measurements but with less variability. The largest EC values are observed in the central part with a mean EC of 6.87 ± 5.34 dS/m. Much lower values are found in the eastern and western parts : 0.81 ±1.41 and 3.30 ± 7.83 dS/m respectively. The most saline subsoils are found close to the Salinas Grandes and Ambargasta reaching values up to 32 dS/m.

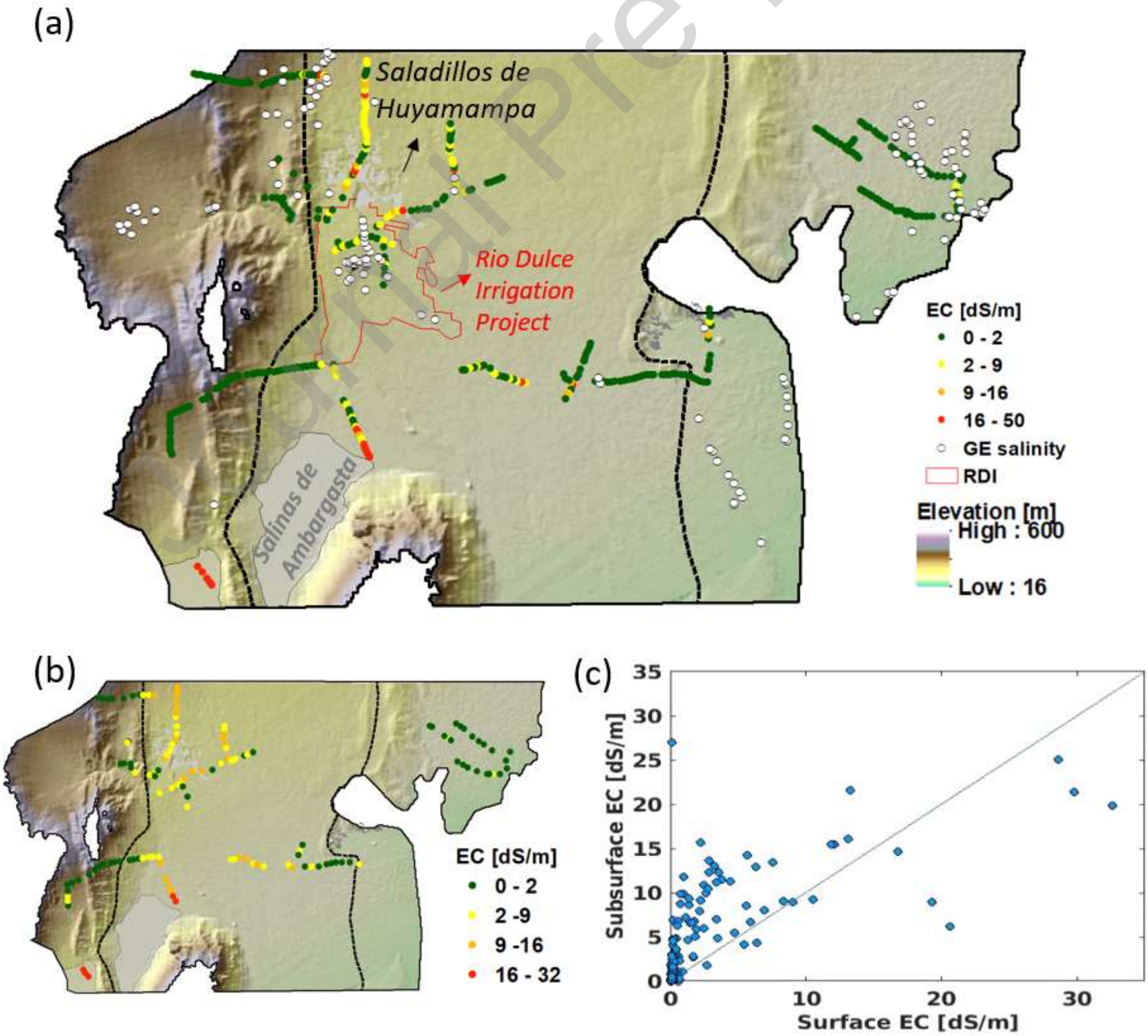

Figure 3: (a) Spatial pattern of surface soil EC values. White dots indicate locations where saline areas where identified based on Google Earth imagery. The red lines show the extent of the Rio Dulce Irrigation Project, (b) same as in (a) but for subsurface EC measurements, (c) relation between the EC of subsurface and corresponding surface samples.

The surface soil salinity is generally low compared to the subsurface EC values (Figure 3c), except for those samples taken in the Salinas where salt crusts are forming as result of evaporation. As shown in Figure 2, salinity crusts in agriculture lands are small and irregular which impedes an accurate detection of the regional pattern of surface salinity. Therefore, the spatial regression analysis was conducted based on the subsurface samples only. The link between surface and subsurface salinity is elaborated in the discussion.

3.2 Subsurface salinity and relation with environmental variables

When analyzing the environmental variables associated to subsurface EC, the *P-Pet*, σ_{GVF} and $DEM_{detrend}$ showed the highest absolute R_{SP} values (and P value < 0.05), and are used in the ensuing regression analysis. The $DEM_{detrend}$ has the highest absolute correlation with EC (-0.50) followed by σ_{GVF} (-0.43) and *P-Pet* (-0.41). The annual mean *SM*, and its temporal standard deviation, have low correlations with EC and are omitted in further analysis, just as the annual mean *GVF* map and σ_{P-Pet}. Scatterplots between the measured EC values of the subsurface soils and the environmental variables are shown in Appendix A.2. The maps of the three selected variables are shown in Figure 4a-c. The *P-Pet* map (Figure 4a) shows a potential water deficit in the central part (mean deficit = -1115 mm/year), in contrast with a lower deficit in the eastern part (mean deficit of -825 mm/year). The western part has a strong north-south deficit-gradient with an annual mean deficit of -1107 mm/year. Figure 4b shows the annual standard deviation of the fraction of ground covered by green vegetation, *GVF*, and represents the vegetation's phenology. The western part, dominated by croplands, has high σ_{GVF} values, reflecting a strong seasonal cycle in vegetation growth. The central part is characterized by low σ_{GVF} values over the Salinas de Amabargasta, the alluvial plain of the Rio Dulce and the Saladillos de Huyamampa. The remaining areas in the central part, mainly consisting of dry forest, have intermediate σ_{GVF} values. The Altos de Otumpa in the east are characterized by high σ_{GVF} , as a result of croplands with strong seasonal cycle. East of Altos de Otumpa, the land cover is dominated by croplands with low σ_{GVF} values. The detrended DEM shows the geomorphological units: the western part has a significantly higher topographic roughness and elevation than the eastern and central part.

In the central part, lower areas correspond to the Salinas de Ambargasta, the Saladillos de Huyamampa and the alluvial plain of the Rio Dulce.

3.3 Regression analysis

The adjusted response plots of the three selected variables (Figure 4d-f) illustrate the relationship between the EC subsurface values and each variable as it was derived by MARS regression over 100 model simulations. The functions describe the relationship between EC and one of the selected environmental variables, whereby the other predictor variables are averaged out. Figure 4d shows a negative relationship between EC and *P-Pet*: the more negative the water balance (higher water deficit), the higher the EC values. The modeled relationship between EC and σ_{GVF} is also negative: areas with low seasonal variability in *GVF* are most likely affected by salinity in the subsurface layers. The relation between $DEM_{detrend}$ and EC is also negative (Figure 4f): topographic lows tend to be more saline.

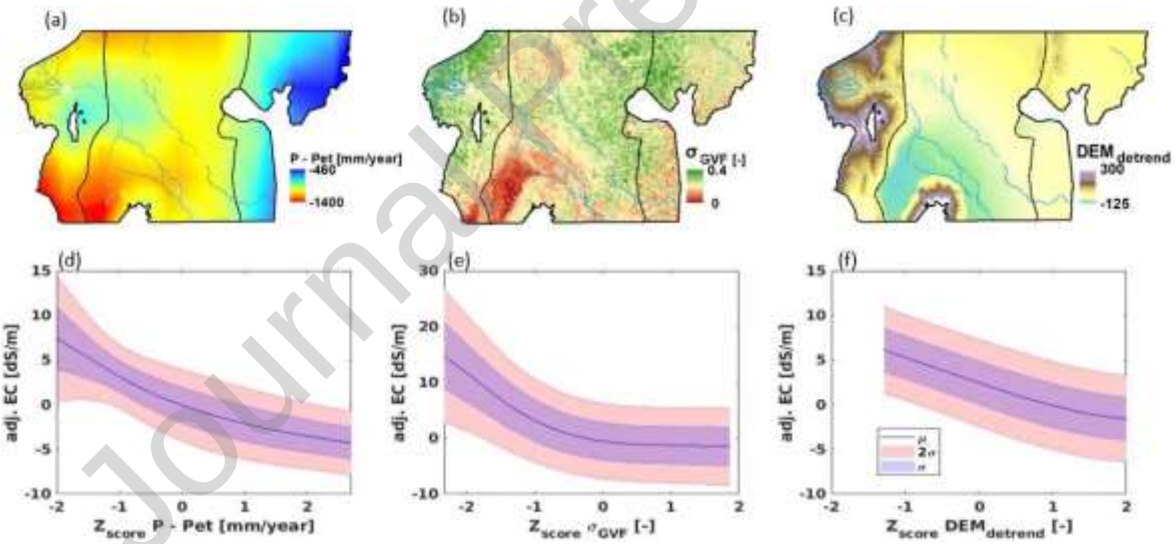

Figure 4: Maps of the (a) annual mean water balance (*P-Pet*), (b) σ_{GVF} and (c) $DEM_{detrend}$. Adjusted response plots between EC and (d) *P-Pet* , (e) σ_{GVF} and (f) $DEM_{detrend}$. The ensemble-mean (blue line) and one (purple) and two (red) standard deviations are shown.

The salinity map (Figure 5a) represents the ensemble-mean of the modeled subsurface EC over the 100 individual regressions. A clear spatial pattern appears: most of the western part is characterized by low salinity values (with mean value of 4.46 dS/m) that increase towards the south (corresponding with the northern edge of Salinas Grandes). The central part is characterized by higher EC values (7.42 dS/m) compared to the western and eastern part. The Salinas de Ambargasta stand out by very high EC values (>32 dS/m), followed by the Saladillos de

Huyamampa and the alluvial plain of the Rio dulce. The eastern part of the Chaco has lower modelled EC values (2.30 dS/cm). The Altos de Otumpa have very low EC values, while east of the Altos de Otumpa, a mosaic of low and intermediate EC values appears. The intermediate EC values often correspond to agriculture plots with low σ_{GVF} values. The low seasonal variation in vegetation growth can be related to reduced crop performance due to soil salinity but also to specific crop management practices (see section 4.2).

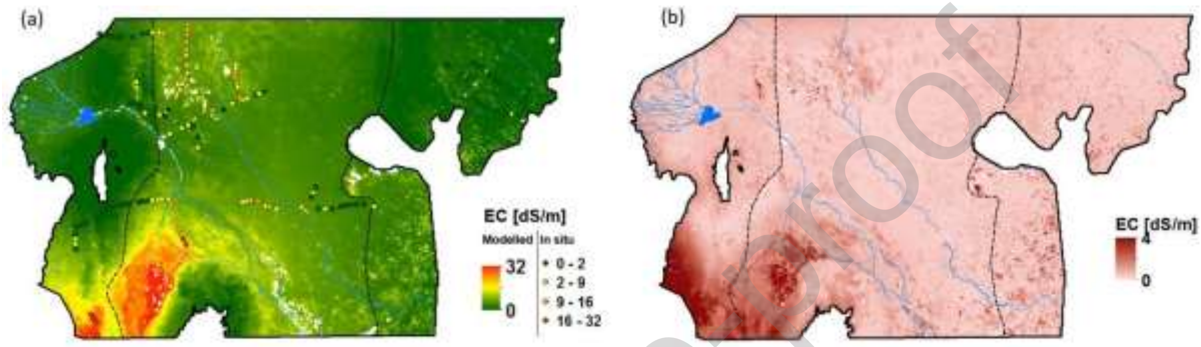

Figure 5: (a) Ensemble mean and (b) standard deviation map of modeled soil salinity (EC) at 1 km resolution, based on 100 simulations.

The uncertainty on the MARS-regression estimates (Figure 5b) are small with a mean value of 0.8 dS/m, indicating that the results are only weakly influenced by selecting different subsets for model calibration. The performance of each ensemble member was assessed by calculating the R^2 and RMSE. Figure 6 shows violin plots whereby each point represents one model simulation (out of 100). The mean R^2 of the calibration and validation dataset are 0.67 and 0.59 respectively, with a larger spread for the validation dataset. Similar results are observed for the RMSE, whereby the mean and standard deviation on the RMSE are lower for the calibration (3.44 ± 0.13 dS/m) compared to the validation dataset (3.66 ± 0.54 dS/m). The average RMSE values (3.44 and 3.66 dS/m for calibration and validation respectively) are larger than the mean ensemble standard deviation (0.8 dS/m). These uncertainty estimates indicate that the uncertainty of the ensemble model underestimates the actual uncertainty. An independent validation dataset would improve the uncertainty assessment and allow us to evaluate the real uncertainties on modeled soil salinity.

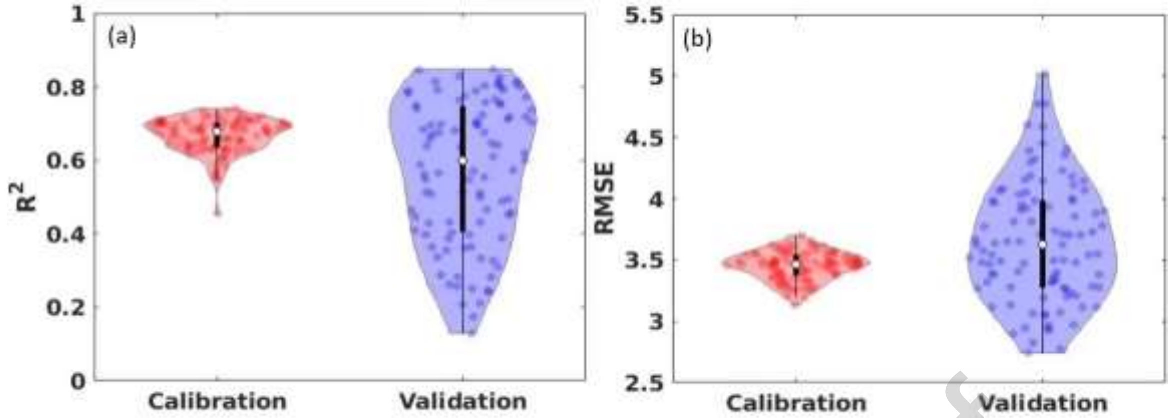

Figure 6: Violin plots of (a) R^2 and (b) RMSE for 100 model simulations. For all simulations, the dataset was randomly divided in a calibration (4/5) and internal validation (1/5) part. Each dot represents a model-member.

4 Discussion

4.1 Spatial patterns of soil salinity over the Dry Chaco

The observed soil salinity pattern is the result of primary and secondary salinization processes (Figure 7). The spatial regression revealed four environmental variables that are associated with the subsurface soil salinity: the annual mean precipitation and potential evapotranspiration (combined in *P-Pet*), the geomorphological setting, and temporal standard deviation in *GVF* (as proxy for vegetation phenology). Below, we discuss the results in the framework of the theoretical concepts of arrested drainage and landscape stagnation (Jobbágy et al., 2020). In appendix A.3, high resolution imagery illustrate the expression of these processes.

4.1.1 Primary salinity: arrested drainage and landscape stagnation

The importance of water deficits (*P-Pet,* R=-0.41) in explaining soil salinity patterns is congruent with the concept of arrested drainage (Jobbágy et al., 2020). In regions with dry to semi-arid climates, there is a restriction of deep drainage as vegetation has the ability to use precipitation inputs exhaustively, either in near-real time or with seasonal or inter-annual deferrals. This mechanism called “arrested drainage” limits water percolation beyond the front of the root zone and favors accumulation of solutes in the upper horizons of the soil mantle. The modeled soil water balances showed the highest water deficits in the central part of the study area (-1115 mm/year), whereas much lower water deficits occur in the eastern part (-825 mm/year). The western part has a strong north-south gradient in water deficit with mean value of -1107 mm/year. These large-scale patterns in soil water balance are also reflected in the subsurface salinity map with mean EC values ranging from 7.42, 2.30 and 4.46 dS/m for the central, eastern and western part respectively. The high water deficits that we report for the central part of the Dry Chaco are likely impeding deep drainage and salt leaching as rainfall inputs (500 to 1000 mm/year) are largely lost through evapotranspiration. Compared to the central part, the higher rainfall inputs in the eastern part result in lower water deficit and higher water excess during the wet season.

The strong association between EC of the subsurface soil horizons and local topography (R=-0.50) is congruent with the concept of landscape stagnation (Jobbágy et al., 2020): flat sedimentary plains such as the Dry Chaco are characterized by low hydraulic gradients and slow subsurface lateral transport of solutes. Even if the arrested drainage condition is not met, the lack of horizontal (ground)water flow in stagnated landscapes efficiently limits the export of salts. The flat topography of the central part is an ideal setting for primary salinity due to landscape stagnation (Figure 7 (1-3), Appendix A.3), where salts accumulate in three large topographic depressions. The Salinas de Ambargasta stand out as the most saline area in the region (Figure 5a). The lake is formed in an endorheic basin: the water inflow mainly consists of saline groundwater that seeps out along tectonic structures (Figueroa et al., 2020). The Saladillos de Huyamampa are likely related to groundwater seepage and blocked drainage in the neighborhood of the Huyamampa Fault. The Rio Dulce's alluvial plain is considered as one of the few remaining saline wetlands (Bucher, 2019). The area is flooded occasionally, and the groundwater table is very close to the surface (Bucher, 2019). The saline open water that accumulates in these topographic depressions is affected by high evaporation rates (caused by the high water deficit) leading to the formation of evaporites.

The eastern part is characterized by high annual mean precipitation (between 1180 and 1684 mm) and flat topography (slopes are generally less than 0.1%) that prevents the effective removal of salts. Groundwater depths in this part of the Chaco are relatively shallow and between 2 and 3 m depth (Giménez et al., 2020a, 2021). The rainfall seasonality is expected to result in seasonally fluctuating groundwater tables. At the end of the rainy season, groundwater tables are highest and salts are mobilized to the upper soil horizons. Soil salinization is expected to occur at the beginning of the dry season when shallow groundwater levels result in capillary rise and direct evaporation of saline groundwater. As long as the dry period lasts, the accumulated salts will be stored in the soil mantle. The majority of subsurface EC measurements taken in the dry season of 2019 were consistently low (0.8 dS/cm), which is attributed to the very wet conditions prior to the field campaign that likely resulted in the dilution of salts.

In contrast to the flat topography of the central Dry Chaco, the western part is located at the margin of the Subandean Ranges: the elevation ranges between 180 and 450 m, and slope gradients are up to 6%. The groundwater is estimated to be at 10 to 40 m depth according to Nicolli et al. (2008), and the main subsurface flow direction is towards the southeast (García et al., 2001). Deforestation is exhaustive (Vallejos et al., 2015, Baumann et al., 2018)) and resulted in effective salt leaching and removal through regional groundwater transport. Locally, higher-than-average EC values and salt crusts are observed corresponding to local topographic depressions with flow convergence and shallow groundwater conditions (Puchulu and Fernández, 2014).

4.1.2 Secondary salinity: land cover changes

Land cover conversions result in deviations from the primary salinity conditions as reported by Amdan et al. (2013); Giménez et al (2016); Marchesini et al. (2017). The impact of anthropogenic change will depend on local hydroclimatic and geomorphological settings conditioning the soil water balance and salt mobilization. Regardless of the original salt concentration in the soil mantle, it is plausible that deforestation in the western part increased deep percolation and salt leaching from the vadose zone to the water table. The risk of severe soil salinization in the near future is likely to be low for the western part: the water table is at depths of 10 to 40 m which does not pose a direct threat for remobilization of salts. According to Amdan et al. (2013), it may take between 30 and 120 years before the rise in the water table affects the upper soil horizons in this part of the Chaco. In addition, it is still unclear whether increased deep percolation will cause groundwater levels to rise as the excess of infiltration water can also be evacuated via regional groundwater flow. Locally, seepage of groundwater along e.g. fault traces or incised valleys can enhance soil salinization (Figure 7 (4a, 6); Appendix A.3). In the central part, where landscape stagnation is likely to occur, the flat topography inhibits salt removal by lateral groundwater flow. It is expected that the hazard of secondary soil salinity will increase with deforestation in the areas that are prone to primary salinity. The shorter the distance to these areas, the shallower the groundwater table, and the higher the risk for capillary rise and mobilization of salts to the soil surface. The eastern part is also characterized by flat topography but is more humid compared to the central part. Flooding events leave visible traces in the form of salt crusts and reduced vegetation growth (Figure 7 (7), Appendix A.3). A study conducted near the village of Bandera, located at the transition between the central and eastern part, indicated that deforested areas show clear signs of groundwater recharge and salt leaching (Giménez et al., 2016). Given the shallow water tables, there is an elevated hazard for severe soil salinization as small increases in deep percolation can result in rapid rise of the water table. The observations from Google Earth imagery support this statement (Figure 7 (4b); Appendix A.2).

Besides deforestation, irrigation schemes artificially change the soil water balance and can enhance secondary salinization (Figure 7 (5); Appendix A.3). The alluvial fan of the Rio Dulce is occupied by numerous small-sized farms for irrigation-fed agriculture. The satellite-based assessment (Figure 3) shows the occurrence of salt patches in numerous agricultural plots, confirming earlier statements by Prieto et al. (2005) about the unsatisfactory performance of the irrigation project.

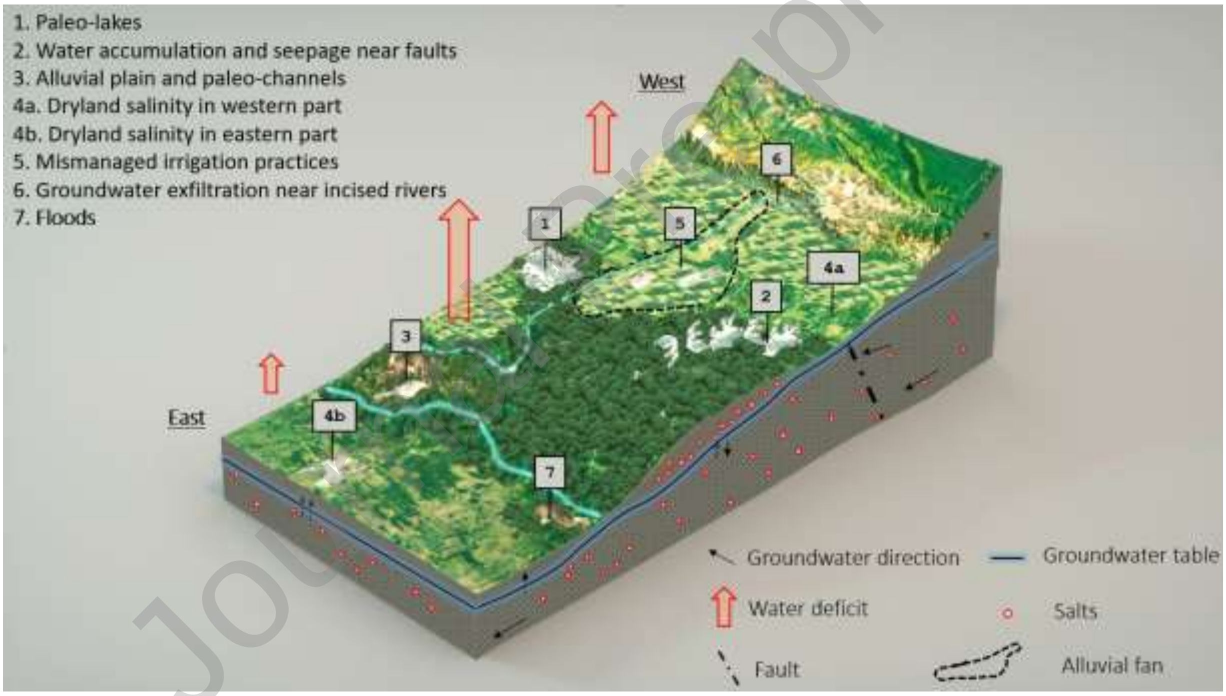

Figure 7: Schematic overview of main processes of soil salinization over the Dry Chaco. High resolution satellite images with visual imprints of the described processes are shown in Appendix A.3.

4.2 Vegetation phenology in relation to soil salinity

In addition to the geomorphological and hydrometeorological controls on soil salinity, we also explored the relation between the EC values and the density of green vegetation (and its seasonal variation represented by σ_{GVF}). The results from the MARS regression show a negative relation between the subsurface EC and the seasonal cycle in *GVF* (represented by σ_{GVF}). This indicates that vegetation can grow to its full potential, when it is not affected by any form of (salt) stress. In contrast, areas with low temporal standard deviations in *GVF*, are characterized by high EC values. Figure 8b shows a scatter density cloud of the σ_{GVF} and the modelled subsurface EC values, classified according to the three major land cover types: forest (n=21588), herbaceous plants (n=4405), and agricultural lands (n=31358) as derived from the ESA-CCI landcover map. The field measurements are plotted with their corresponding σ_{GVF}. Figure 8b illustrates that dry forests have intermediate σ_{GVF} and EC values. They have relatively high annual means of *GVF*, but without much variability throughout the year and tend to present high subsurface EC values from arrested drainage conditions. Herbaceous vegetation with lower σ_{GVF} values is predominant on soils with EC values above 15 dS/m. These areas with halophytic vegetation have low variability in *GVF* over the year. The scatter density cloud illustrates the interaction between plant functional types and soil salinity, where plant types and phenological activity differ with soil salinity.

Anthropogenic activities can create secondary salinization (Figure 8). Deforestation can lead to an increase in the σ_{GVF} as croplands are characterized by a higher seasonality in *GVF* compared to forests and herbaceous plants. Croplands with above-average σ_{GVF} values have modelled EC values below 5 dS/m, illustrating that conversion from forest to agriculture induces salt leaching. The results also show that croplands with higher soil EC values are associated with lower σ_{GVF} . Although this could be interpreted as the first effects of secondary salinization on crop growth as low σ_{GVF} values can be the result of poor crop performance, the results need to be interpreted with caution as intensified cropping systems (with e.g. highly productive double-crop systems) could also result in constantly high *GVF* (Giménez et al., 2020b). It must be mentioned that the use of σ_{GVF} as an explanatory variable in the regression model, introduces a certain degree of endogeneity, since σ_{GVF} is affected by soil salinity conditions and not the other way around. However, it is considered that the approach and setup used adds value in providing a complete picture of soil salinity processes in the region.

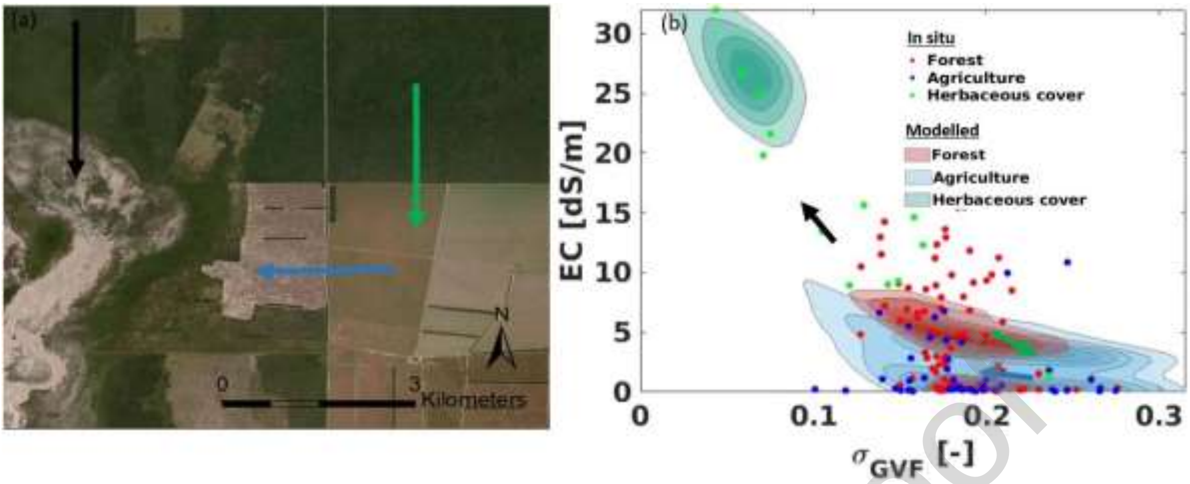

Figure 8: (a) The association between soil salinity and vegetation density as observed in Google Earth imagery. The black arrow shows spatial gradients in vegetation density and soil salt crusts as they occur in natural vegetation, while the green and blue arrows illustrate the effect of deforestation on secondary salinization. (b) Relation between the modelled subsurface EC values and the seasonal variation in the density of green vegetation, σ_{GVF} . The data are classified according to land cover type. In soils with higher salinity, salt-tolerant herbaceous plants become dominant showing low σ_{GVF}. Agricultural plots typically show lower EC values than forests (green arrow), although there exists large variability in the EC values which could be indicative of dryland salinization, EC increase and σ_{GVF} decrease (blue arrow).

4.3 Uncertainties and scope for further research

The regional assessment provides insights into the spatial pattern of soil salinity and the salinization processes across the Dry Chaco. The regional assessment of soil salinity can be further improved by resolving the following data and model uncertainties. First, there is a spatial mismatch between our point-measurements and the 1 km resolution of the final salinity-map, whereby the point measurements are not fully representative for the 'real' EC value of the entire pixel. The representativeness of the in-situ salinity measurements can be addressed by studying the spatial variability of soil salinity measurements at the 1-km scale. Second, time series analyses of soil salinity, groundwater level and water quality data can contribute to unravel the intra- and inter-annual variations in soil salinity. In this study, the EC measurements were taken during the 2019 dry season and contain imprints of first, second and third order temporal variability. The intra- and inter-annual variations due to e.g. precipitation events were not fully accounted for in the hydrometeorological and vegetation data. Continuous monitoring of soil salinity, groundwater level and water quality across the Dry Chaco will remain important. Given the extensiveness of this data-scarce region, land surface models combined with satellite retrievals and field data from monitoring networks may provide complementary information.

Recent advances in the detection of shallow groundwater tables based on space-borne soil moisture observations can be promising for future regional salinity assessments (Soylu and Bras, 2021). Third, a comprehensive analysis of salinity variations with depth is needed to evaluate the soil salinity hazard over the Dry Chaco. Recent work by Jobbágy et al. (2020) stated that soil profiles under natural vegetation can display a strong increase in salt content below the first or second meter. Therefore, a regional salinity map based on samples taken in the upper 1 m of soil material might underestimate the overall salinity hazard. Besides, Jobbágy et al. (2011) found that soil texture also plays an important role in determining the salinization hazard as soil chloride accumulation was not observed in much drier but extremely sandy environments. Future work is needed to quantify soil salinity variations with depth and how it relates to soil texture, as this will be informative for understanding the salinization processes.

5 Conclusions

This study on the geographic distribution of soil salinity over the central Dry Chaco is based on 492 surface and 142 subsurface soil electrical conductivity (EC) measurements taken along multiple east-west transects covering the existing topographic and climatic gradients across the region. The subsurface EC values were systematically higher than the surface values and showed clear regional patterns. The study provides answers to the research questions raised in the introduction section. First, subsurface salinity is closely related to the annual water budget (represented as *P-Pet*), topography and vegetation phenology. Second, remotely-sensed vegetation indices such as the seasonal variation in the density of green vegetation, σ_{GVF} , were shown to be particularly suitable for identifying primary soil salinity at regional scale. Third, the geographic distribution of soil salinity can be explained by the concepts of arrested drainage and landscape stagnation. In flat areas with high water deficit, corresponding with the central part of the Chaco, salts are retained in the soil profile and prevented from leaching. Severe natural soil salinization occurs when groundwater accumulates near the surface and high evapotranspiration leads to the formation of evaporites. This is the case in topographic depressions due to tectonic activity or alluvial plains. Low natural salinity is observed in regions with higher slope gradients (western Chaco), as salts are effectively removed from the landscape by regional groundwater transport. Low salinity is also observed in areas with higher precipitation due to salt leaching (eastern Chaco). However, our data also showed how these wetter parts are susceptible for secondary salinization following deforestation due to their shallow groundwater tables.

A critical issue in the analysis of dryland salinization remains the time lag between land use change and the actual or perceived onset of environmental degradation, as shifts in soil water balance and soil salinization are the consequences of land use changes that occurred years to decades earlier. Because of this time lag and the uncertainty on future deforestation in the Chaco, it is difficult to predict how fast dryland salinization will evolve in the future. Our results indicate that the extent of future dryland salinization in the Dry Chaco will mainly depend on whether areas prone to natural soil salinity are further protected from deforestation (the wide surroundings of topographic depressions where shallow groundwater tables occur in combination with high water deficits), and on the magnitude and rate of groundwater rise after deforestation. Our findings show that this will be dependent on the local climate and geomorphology that determine the depth of the groundwater table. These results can provide a basis for further research on the spatial variations of natural and secondary salinity in dryland ecosystems and the development of adequate land use planning and groundwater/salinity monitoring network

References

Adnan, R. M., Liang, Z., Heddam, S., Zounemat-Kermani, M., Kisi, O., and Li, B.: Least square support vector machine and multivariate adaptive regression splines for streamflow prediction in mountainous basin using hydro-meteorological data as inputs, Journal of Hydrology, 586, 124 371, https://doi.org/10.1016/j.jhydrol.2019.124371, 2020.

Allbed, A. and Kumar, L.: Soil salinity mapping and monitoring in arid and semi-arid regions using remote sensing technology: a review, Advances in Remote Sensing, 2, 373–385, 2013.

Allen, R. G., Pereira, L. S., Raes, D., and Smith, M.: Crop evapotranspiration: guidelines for computing crop water requirements, FAO irrigation and drainage paper 56, FAO, Rome, Italy, 1998.

Amdan, M., Aragón, R., Jobbágy, E., Volante, J. N., and Paruelo, J. M.: Onset of deep drainage and salt mobilization following forest clearing and cultivation in the Chaco plains (Argentina), Water Resources Research, 49, 6601–6612, 2013.

Baumann, M., Levers, C., Macchi, L., Bluhm, H., Waske, B., Gasparri, N.I., and Kuemmerle, T.: Mapping continuous fields of tree and shrub cover across the Gran Chaco using Landsat 8 and Sentinel-1 data, Remote Sensing of Environment, 216, 201-211,2018.

Bhattacharya, P., Claesson, M., Bundschuh, J., Sracek, O., Fagerberg, J., Jacks, G., Martin, R. A., Storniolo, A. d. R., and Thir, J. M.: Distribution and mobility of arsenic in the Rio Dulce alluvial aquifers in Santiago del Estero Province, Argentina, Science of the Total Environment, 358, 97–120, 2006.

Bucher, E. and Huszar, P. C.: Sustainable management of the Gran Chaco of South America: ecological promise and economic constraints, Journal of Environmental Management, 57, 99–108, 1999.

Bucher, E. H.: Dulce River Wetland, in: The Mar Chiquita Salt Lake (Córdoba, Argentina), pp. 97–109, Springer, 2019.

Clark, M. L., Aide, T. M., Grau, H. R., and Riner, G.: A scalable approach to mapping annual land cover at 250 m using MODIS time series data: A case study in the Dry Chaco ecoregion of South America, Remote Sensing of Environment, 114, 2816–2832, 2010.

Daliakopoulos, I., Tsanis, I., Koutroulis, A., Kourgialas, N., Varouchakis, A., Karatzas, G., and Ritsema, C.: The threat of soil salinity: A European scale review, Science of the Total Environment, 573, 727–739, 2016.

De Marzo, T., Pflugmacher, D., Baumann, M., Lambin, E. F., Gasparri, I., and Kuemmerle, T.: Characterizing forest disturbances across the Argentine Dry Chaco based on Landsat time series, International Journal of Applied Earth Observation and Geoinformation, 98, 102 310, https://doi.org/10.1016/j.jag.2021.102310, 2021.

Domenico, P. A. and Schwartz, F. W.: Physical and chemical hydrogeology, Wiley, New York (N.Y.), 2nd edition., 1998.

Ek, M., Mitchell, K., Lin, Y., Rogers, E., Grunmann, P., Koren, V., and Gayno, G.: Implementation of Noah Land Surface Model Advances in the National Centers for Environmental Prediction Operational Mesoscale Eta Model, Journal of Geophysical Research, 108, 8851, https://doi.org/10.1029/2002JD003296, 2003.

Fan, X., Pedroli, B., Liu, G., Liu, Q., Liu, H., and Shu, L.: Soil salinity development in the yellow river delta in relation to groundwater dynamics, Land Degradation & Development, 23, 175–189, 2012.

Figueroa, M. E., Lorenz, G., and Giménez, A. M.: An Ecological Overview of Halophytes from Arid Inland Environments of Argentina, Handbook of Halophytes: From Molecules to Ecosystems towards Biosaline Agriculture, pp. 1–23, 2020.

Friedman, J.: Multivariate Adaptive Regression Splines, The Annals of statistics, 19, 1–67, 1991.

Furby, S., Caccetta, P., and Wallace, J.: Salinity monitoring in Western Australia using remotely sensed and other spatial data, Journal of environmental quality; 39, 16–25, 2010

García, G. M., Hidalgo, M. d. V., and Blesa, M. A.: Geochemistry of groundwater in the alluvial plain of Tucuman province, Argentina, Hydrogeology Journal, 9, 597–610, 2001.

Gasparri, N. I.: The transformation of land-use competition in the Argentinean Dry Chaco between 1975 and 2015, in: Land Use Competition, pp. 59–73, Springer, 2016.

Gasparri, N. I. and Grau, H. R.: Deforestation and fragmentation of Chaco dry forest in NW Argentina (1972–2007), Forest Ecology and Management, 258, 913–921, 2009.

Gelaro, R., McCarty, W., Súarez, M. J., Todling, R., Molod, A., Takacs, L., Randles, C. A., Darmenov, A., Bosilovich, M. G., Reichle, R., et al.: The modern-era retrospective analysis for research and applications, version 2 (MERRA-2), Journal of Climate, 30, 5419–5454, 2017.

Giménez, R., Mercau, J., Nosetto, M., Páez, R., and Jobbágy, E.: The ecohydrological imprint of deforestation in the semiarid Chaco: insights from the last forest remnants of a highly cultivated landscape, Hydrological Processes, 30, 2603–2616, 2016.

Giménez, R., Mercau, J., Schultz, W., Scheffer, E.: Dinámica de la napa freática en sistemas agrícolas del Chaco semiárido bajo diferentes secuencias de cultivo, in: XXVII Congreso Argentino de la Ciencia del Suelo, 2020a.

Giménez, R., Mercau, J. L., Bert, F. E., Kuppel, S., Baldi, G., Houspanossian, J., Magliano, P. N., and Jobbágy, E. G.: Hydrological and productive impacts of recent land-use and land-cover changes in the semiarid Chaco: Understanding novel water excess in water scarce farmlands, Ecohydrology, 13, e2243, https://doi.org/10.1002/eco.2243, 2020b.

Giménez, R., Schultz, W., de Rosas, J., Lopez, E.: FreatChaco: Red Colaborativa de Monitoreo de la napa freática del sudoeste de Chaco., in: XIII Congreso Argentino de Agroinformática, 2021.

Glatzle, A., Reimer, L., Núñez-Cobo, J., Smeenk, A., Musálem, K., and Laino, R.: Groundwater dynamics, land cover and salinization in the dry Chaco in Paraguay, Ecohydrology & Hydrobiology, 20, 175–182, 2020.

Gobbi, B., Van Rompaey, A., Loto, D., Gasparri, I., and Vanacker, V.: Comparing Forest Structural Attributes Derived from UAV-Based Point Clouds with Conventional Forest Inventories in the Dry Chaco, Remote Sensing, 12, 4005, 2020.

Gutiérrez, A. A., Mon, R., Sábat, F., and Iaffa, D.: Origin and Evolution of the Salinas Grandes and Salina De Ambargasta, Argentina, in: IOP Conference Series: Earth and Environmental Science, vol. 95, p. 022036, IOP Publishing, 2017.

Gutiérrez, M. and Johnson, E.: Temporal variations of natural soil salinity in an arid environment using satellite images, Journal of South American Earth Sciences, 30, 46–57, 2010.

Hansen, M. C., Potapov, P. V., Moore, R., Hancher, M., Turubanova, S. A., Tyukavina, A., Thau, D., Stehman, S., Goetz, S. J., Loveland, T. R., et al.: High-resolution global maps of 21st-century forest cover change, Science, 342, 850–853, 2013.

Hopmans, J. W., Qureshi, A., Kisekka, I., Munns, R., Grattan, S., Rengasamy, P., Ben-Gal, A., Assouline, S., Javaux, M., Minhas, P., et al.: Critical knowledge gaps and research priorities in global soil salinity, Advances in Agronomy, p. 191, 2021.

Jekabsons, G.: ARESLab: Adaptive Regression Splines Toolbox for Matlab/Octave. Technical Report, 2016.

Jobbágy, E. G. and Jackson, R. B.: Groundwater use and salinization with grassland afforestation, Global Change Biology, 10, 1299–1312, 2004.

Jobbágy, E. G., Nosetto, M. D., Villagra, P. E., and Jackson, R. B.: Water subsidies from mountains to deserts: Their role in sustaining groundwater-fed oases in a sandy landscape, Ecological Applications, 21, 678–694, 2011.

Jobbágy, E. G., Giménez, R., Marchesini, V., Diaz, Y., Jayawickreme, D. H., and Nosetto, M. D.: Salt Accumulation and Redistribution in the Dry Plains of Southern South America: Lessons from Land Use Changes, in: Saline and Alkaline Soils in Latin America, pp. 51–70, Springer, 2020.

Kirches, G., Brockmann, C., Boettcher, M., Peters, M., Bontemps, S., Lamarche, C., Schlerf, M., Santoro, M., and Defourny, P.: Land Cover CCI-Product User Guide-Version 2, 2014.

Kisi, O. and Parmar, K. S.: Application of least square support vector machine and multivariate adaptive regression spline models in long term prediction of river water pollution, Journal of

Hydrology, 534, 104–112, 2016.

Kumar, S. V., Peters-Lidard, C. D., Eastman, J. L., and Tao, W.-K.: An integrated high- resolution hydrometeorological modeling testbed using LIS and WRF, Environmental Modelling & Software, 23, 169–181, 2008.

Lambers, H.: Introduction, Dryland Salinity: A Key Environmental Issue in Southern Australia, Plant and Soil, 257, 5–7, 2003.

Latrubesse, E. M., Stevaux, J. C., Cremon, E. H., May, J.-H., Tatumi, S. H., Hurtado, M. A., Bezada, M., and Argollo, J. B.: Late Quaternary megafans, fans and fluvio-aeolian interactions in the Bolivian Chaco, Tropical South America, Palaeogeography, Palaeoclimatology, Palaeoecology, 356, 75–88, 2012.

Leeder, M. and Gawthorpe, R.: Sedimentary models for extensional tilt-block/half-graben basins, Geological Society, London, Special Publications, 28, 139–152, 1987.

Lobell, D., Lesch, S., Corwin, D., Ulmer, M., Anderson, K., Potts, D., Doolittle, J., Matos, M., and Baltes, M.: Regional-scale assessment of soil salinity in the Red River Valley using multi-year MODIS EVI and NDVI, Journal of Environmental Quality, 39, 35–41, 2010.

Maertens, M., De Lannoy, G. J. M., Apers, S., Kumar, S. V., and Mahanama, S. P. P.: Land surface modeling over the Dry Chaco: the impact of model structures, and soil, vegetation and land cover parameters, Hydrology and Earth System Sciences, 25, 4099–4125, https://doi.org/10.5194/hess-25-4099-2021, 2021.

Marchesini, V. A., Giménez, R., Nosetto, M. D., and Jobbágy, E. G.: Ecohydrological transformation in the Dry Chaco and the risk of dryland salinity: Following Australia's footsteps?, Ecohydrology, 10, e1822, https://doi.org/10.1002/eco.1822, 2017.

Massart, S.: Simulated and observed spatial patterns of soil moisture over the Dry Chaco, Argentina, KU Leuven. Faculteit Bio-Ingenieurswetenschappen, 2020.

Metternicht, G. and Zinck, J.: Remote sensing of soil salinity: potentials and constraints, Remote Sensing of Environment, 85, 1–20, 2003.

Minetti, J. L., Albarracín, S. A., Bobba, M. E., Hernández, C. M., López, E. R., Acunã, L. A., Costa, M. C., Nieva, I. J., and Mendoza, E.: Atlas climático del noroeste argentino, 1999.

Miro, R. and Gonfiantini, R.: Investigación Isotópica del Agua Subterranea en el área de Santiago del Estero, República Argentina, Servicio Nacional Minero-Geológico e International Atomic Energy. Santiago del Estero, Argentina-Viena, Austria, 1980.

Mon, R. and Gutiérrez, A. A.: The Mar Chiquita Lake: An indicator of intraplate deformation in the central plain of Argentina, Geomorphology, 111, 111–122, 2009.

Moretti, L. M., Morrás, H. J. M., Pereyra, F. X., and Schulz, G. A.: Soils of the Chaco Region, in: The Soils of Argentina, pp. 149–160, Springer, 2019.

Munns, R.: Genes and salt tolerance: bringing them together, New phytologist, 167, 645–663, 2005.

Nicolli, H., Tineo, A., Falcón, C., García, J., Merino, M., Etchichury, M., Alonso, M., and Tofalo, O.: Arsenic hydrogeochemistry in groundwater from the Burruyacú basin, Tucumán province, Argentina, Natural arsenic in groundwater of Latin America. In: Bundschuh J, Bhattacharya P., Arsenic in the environment, Boca Raton: CRC Press, Balkema, 1, 47–59, 2008.

Nosetto, M., Jobbágy, E., Tóth, T., and Jackson, R.: Regional patterns and controls of ecosystem salinization with grassland afforestation along a rainfall gradient, Global Biogeochemical Cycles, 22, https://doi.org/10.1029/2007GB003000, 2008.

Nosetto, M. D., Acosta, A., Jayawickreme, D., Ballesteros, S., Jackson, R., and Jobbágy, E.: Land-use and topography shape soil and groundwater salinity in central Argentina, Agricultural Water Management, 129, 120–129, 2013.

Peña-Angulo, D., Vicente-Serrano, S., Domínguez-Castro, F., Noguera, I., Tomas-Burguera, M., López-Moreno, J., Lorenzo-Lacruz, J., and El Kenawy, A.: Unravelling the role of vegetation on the different trends between climatic and hydrologic drought in headwater catchments of Spain, Anthropocene, 36, 100 309, 2021.

Pennington, J. T. and Chavez, F. P.: Seasonal fluctuations of temperature, salinity, nitrate, chlorophyll and primary production at station H3/M1 over 1989–1996 in Monterey Bay, California, Deep Sea Research Part II: Topical Studies in Oceanography, 47, 947–973, 2000.

Peri, V. G.: Caracterización morfotectónica de las Lomadas de Otumpa (Gran Chaco, Santiago del Estero y Chaco): influencias en el control del drenaje, Ph.D. thesis, Facultad de Ciencias Exactas y Naturales. Universidad de Buenos Aires, 2012.

Prieto, D.: Modernization and the evolution of irrigation practices in the Rio Dulce Irrigation Project, Santiago del Estero, Argentina: una tarea de todos, Wageningen Agricultural University, Department of Irrigation and Soil and Water Conservation, the Netherlands, 2006.

Prieto, D., Angella, G., Angueira, M. C., Carrera, A. P., and Moscuzza, C.: Indicadores de desempenõ del sistema de riego del Rio Dulce, Santiago del Estero, Argentina, in: Uso y gestión del Agua en Tierras Secas, 11, pp. 55–78, CYTED, 2005.

Puchulu, M. E. and Fernández, D. S.: Características y distribución espacial de los suelos de la provincia de Tucumán, Geología de Tucumán, pp. 1–17, 2014.

Ramos, V. A., Cristallini, E. O., and Pérez, D. J.: The Pampean flat-slab of the Central Andes, Journal of South American Earth Sciences, 15, 59–78, 2002.

Reichle, R. H., Draper, C. S., Liu, Q., Girotto, M., Mahanama, S. P., Koster, R. D., and De Lannoy, G. J.: Assessment of MERRA-2 land surface hydrology estimates, Journal of Climate, 30, 2937–2960, 2017.

Rengasamy, P.: World salinization with emphasis on Australia, Journal of Experimental Botany, 57, 1017–1023, 2006.

Richards, L. A.: Diagnosis and Improvement of Saline and Alkali Soils, vol. 78, 1954.

Roberts, D. R., Bahn, V., Ciuti, S., Boyce, M. S., Elith, J., Guillera-Arroita, G., Hauenstein, S., Lahoz-Monfort, J. J., Schöder, B., and Thuiller, W.: Cross-validation strategies for data with temporal, spatial, hierarchical, or phylogenetic structure, Ecography, 40, 913–929, 2017.

Rounaghi, M. M., Abbaszadeh, M. R., and Arashi, M.: Stock price forecasting for companies listed on Tehran stock exchange using multivariate adaptive regression splines model and semi-parametric splines technique, Physica A: Statistical Mechanics and its Applications, 438, 625–633, 2015.

Roy, S. S., Roy, R., and Balas, V. E.: Estimating heating load in buildings using multivariate adaptive regression splines, extreme learning machine, a hybrid model of MARS and ELM, Renewable and Sustainable Energy Reviews, 82, 4256–4268, 2018.

Rueda, C. V., Baldi, G., Gasparri, I., and Jobbágy, E. G.: Charcoal production in the Argentine Dry Chaco: Where, how and who?, Energy for Sustainable Development, 27, 46–53, 2015.

Schofield, R., Thomas, D. S., and Kirkby, M. J.: Causal processes of soil salinization in Tunisia, Spain and Hungary, Land Degradation & Development, 12, 163–181, 2001.

Scudiero, E., Skaggs, T. H., and Corwin, D. L.: Regional scale soil salinity evaluation using Landsat 7, western San Joaquin Valley, California, USA, Geoderma, 2, 82–90, 2014a.

Scudiero, E., Teatini, P., Corwin, D. L., Ferro, N. D., Simonetti, G., and Morari, F.: Spatiotemporal response of maize yield to edaphic and meteorological conditions in a saline farmland, Agronomy Journal, 106, 2163–2174, 2014b.

Scudiero, E., Skaggs, T. H., and Corwin, D. L.: Regional-scale soil salinity assessment using Landsat ETM+ canopy reflectance, Remote Sensing of Environment, 169, 335–343, 2015.

*S*mets, B., Jacobs, T., Swinnen, E., Toté, C., and Wolfs, D.: Product User Manual Normalized Difference Vegetation Index (NDVI), Operation of the Global Land Component", Copernicus, 2016.

Soylu, M. E. and Bras, R. L.: Detecting Shallow Groundwater from Spaceborne Soil Moisture Observations, Water Resources Research, 57, e2020WR029 102, https://doi.org/10.1029/2020WR029102, 2021.

Taghizadeh-Mehrjardi, R., Minasny, B., Sarmadian, F., and Malone, B.: Digital mapping of soil salinity in Ardakan region, central Iran, Geoderma, 213,15–28, 2014

Taghizadeh-Mehrjardi, R., Schmidt, K., Toomanian, N., Heung, B., Behrens, T., Mosavi, A., Band, S. S., Amirian-Chakan, A., Fathabadi, A., and Scholten, T.: Improving the spatial prediction of soil salinity in arid regions using wavelet transformation and support vector regression models, Geoderma, 383, 114 793, 2021.

Thalmeier, M. B., Kröhling, D. M., and Brunetto, E.: The geomorphology and Late Quaternary sedimentary record of the Salado/Juramento fluvial megafan, Central Andes foreland basin (Chaco Plain, Argentina), Geomorphology, 373, 107 495, 2021.

Trnka, M., Kersebaum, K. C., Eitzinger, J., Hayes, M., Hlavinka, P., Svoboda, M., Dubrovsky, M., Semeradova, D., Wardlow, B., and Pokorny, E.: Consequences of climate change for the soil climate in Central Europe and the central plains of the United States, Climatic Change, 120, 405–418, 2013.

Turnbull, L., Wilcox, B. P., Belnap, J., Ravi, S., D'odorico, P., Childers, D., Gwenzi, W., Okin, G., Wainwright, J., Caylor, K., et al.: Understanding the role of ecohydrological feedbacks in ecosystem state change in drylands, Ecohydrology, 5, 174–183, 2012.

Vallejos, M., Volante, J. N., Mosciaro, M. J., Vale, L. M., Bustamante, M. L., and Paruelo, J. M.: Transformation dynamics of the natural cover in the Dry Chaco ecoregion: a plot level geo-database from 1976 to 2012, Journal of Arid Environments, 123, 3–11, 2015.

Vanacker, V., Linderman, M., Lupo, F., Flasse, F., and Lambin, E.: Impact of short-term rainfall fluctuation on interannual land cover change in sub-Saharan Africa, Global Ecology and Biogeography, 14, 123-135, 2005.

Vincent, F., Maertens, M., Bechtold, M., Jobbágy, E., Reichle, R. H., Vanacker, V., Vrugt, J., Wigneron, J.-P., and De Lannoy, G. J. M.: Evaluating soil salinity, soil moisture and vegetation estimates in the Dry Chaco using field data, model simulations and L-band satellite observations, Remote Sensing of Environment (In Review), 2021.

Walker, G. R., Gilfedder, M., and Williams, J.: Effectiveness of current farming systems in the control of dryland salinity, Commonwealth Scientific and Industrial Research Organisation, Land and Water, Canberra, Australia, 1999.

Wu, W., Al-Shafie, W. M., Mhaimeed, A. S., Ziadat, F., Nangia, V., and Payne, W. B.: Soil salinity mapping by multiscale remote sensing in Mesopotamia, Iraq, IEEE Journal of Selected Topics in Applied Earth Observations and Remote Sensing, 7, 4442–4452, 2014.

Yamazaki, D., Ikeshima, D., Sosa, J., Bates, P. D., Allen, G. H., and Pavelsky, T. M.: MERIT Hydro: a high-resolution global hydrography map based on latest topography dataset, Water Resources Research, 55, 5053–5073, 2019.

Zhang, T.-T., Zeng, S.-L., Gao, Y., Ouyang, Z.-T., Li, B., Fang, C.-M., and Zhao, B.: Using hyperspectral vegetation indices as a proxy to monitor soil salinity, Ecological Indicators, 11, 1552–1562, 2011.

Zhang, T.-T., Qi, J.-G., Gao, Y., Ouyang, Z.-T., Zeng, S.-L., and Zhao, B.: Detecting soil salinity with MODIS time series VI data, Ecological Indicators, 52, 480–489, 2015.

A Appendices

A.1 Identification of saline topsoils on Google Earth imagery

As mentioned in section 2.2, the identification of salt-crusts on agriculture plots was hindered to their small irregular shape and the wet period prior to the field campaign. To gain more insights into their spatial distribution, Google Earth imagery was consulted to localize salt crusts across the study area. Based on the differences in surface reflectance between salt and non-salt affected areas, salt crusts at the soil's surface were detected. Note that their identification can be complicated and may yield unreliable results when soil moisture is high or the crusts contain other soil constituents. Therefore, the 'historical imagery' function in Google Earth was used, allowing to monitor soil conditions over multiple years. We mainly focused on images of the period 2013-2019. The criteria to separate salt and non-salt affected areas on high resolution satellite-imagery is shown in Figure A.1.

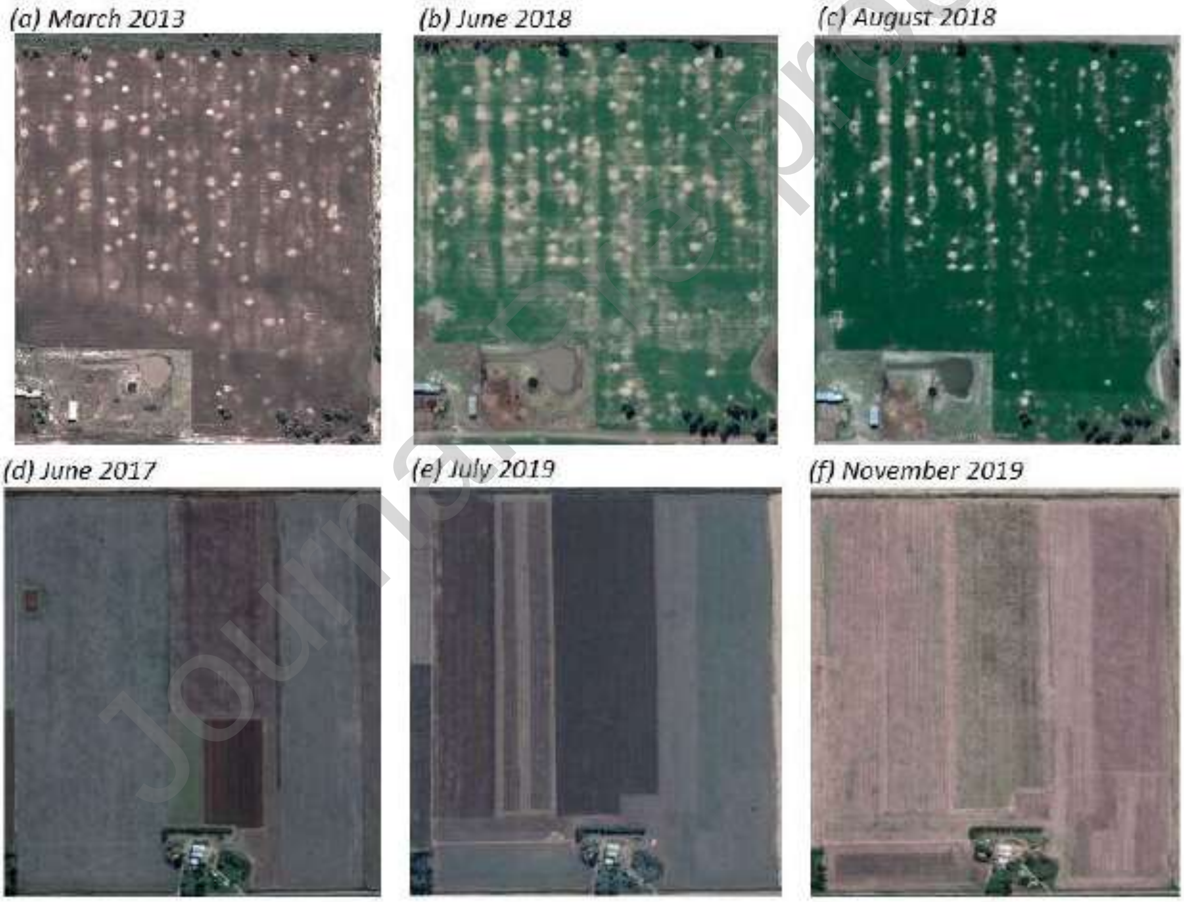

Figure A.1: Illustration of differences in surface reflectance for salt (a-c) and non-salt affected cropland (d-f) as observed on Google Earth Imagery over multiple years.

Figures a-c show an agriculture plot that was considered as saline based on the appearance of white irregular patches across the field. The color of the spots evolves over time (ranging from white to brown) but their location is relatively fixed. For comparison, Figures d-f show an agriculture plot without any signs of soil salinity. It is important to mention that most of the spots identified on Google Earth were not validated in the field. Consequently, the used approach only identified areas that are `most likely' saline topsoils.

A.2 Soil salinity and its relation with environmental variables

The relation between EC and the selected environmental variables is shown in Figure A.2.1. Note that the relation between EC, *LAI* and σ_{LAI} is not shown due to the high multicollinearity between *LAI* and *GVF* (VIF > 3). In each scatterplot, the Spearman correlation coefficient and P value are also shown. The *P-Pet*, σ_{GVF} and $DEM_{detrend}$ have an absolute $R_{SP} \geq 0.40$ and P value < 0.05, and were used in the regression analysis (variables are indicated in red). The $DEM_{detrend}$ has the highest absolute correlation with EC (-0.50) followed by σ_{GVF} (-0.43) and *P-Pet* (-0.41). The other variables show low correlations with EC and were omitted in further analysis.

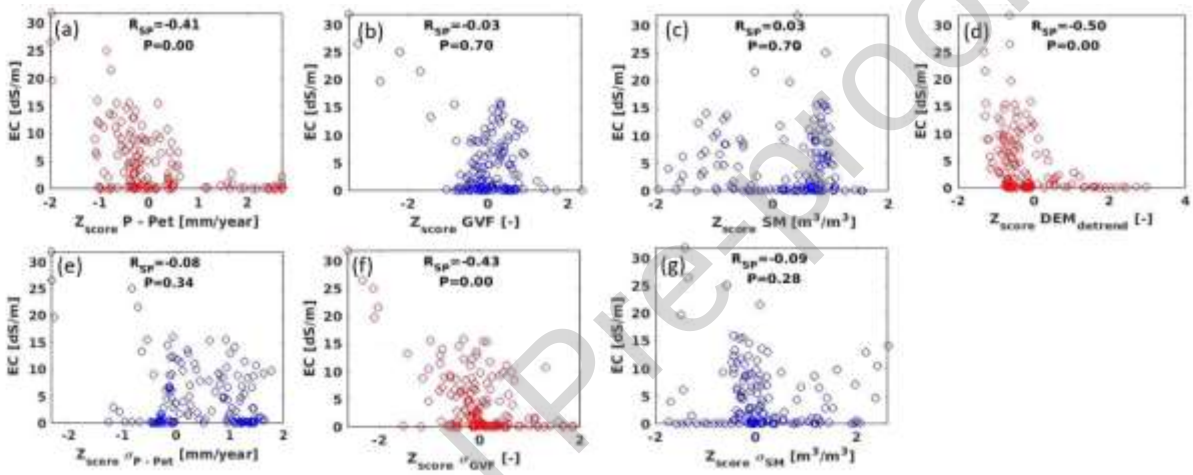

Figure A.2.1: Scatterplots between the EC values of the subsurface soil samples and environmental variables with indication of the Spearman correlation coefficient (R_{SP}) and P value. Variablesin red are used in the spatial interpolation (regression) analysis.

It was also verified if the spatial coverage of visited areas during the field campaign were representative for the entire study area. The spatial distribution of the environmental variables over the entire study area was compared with the one of the sampling points (Figure A.2.2a-c). The bars in Figure A.2.2 a-c represent the distribution of the environmental variables for the sampling points (green bars) and the entire study area (gray bars). The histograms illustrate that the EC dataset covers most of the study area's variability for the three selected variables. This is confirmed by the student's t-values indicating that the null-hypothesis of the t-test cannot be rejected and that the mean differences in the distributions are not significant.

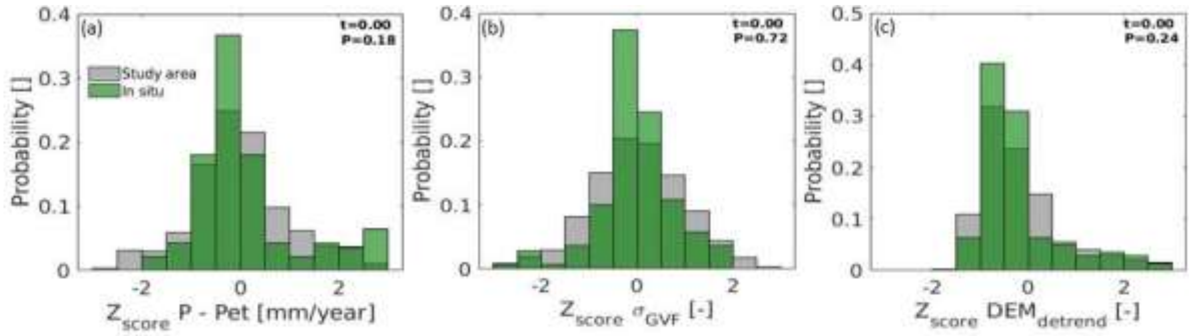

Figure A.2.2: Histograms representing the distribution of the 1-km environmental variables for the sampling points (green bars) and the entire study area (gray) for (a) *P-Pet*, (b) σ_{GVF} and (c) DEM$_{detrend}$ respectively.

A.3 Different salinity processes as observed on satellite imagery

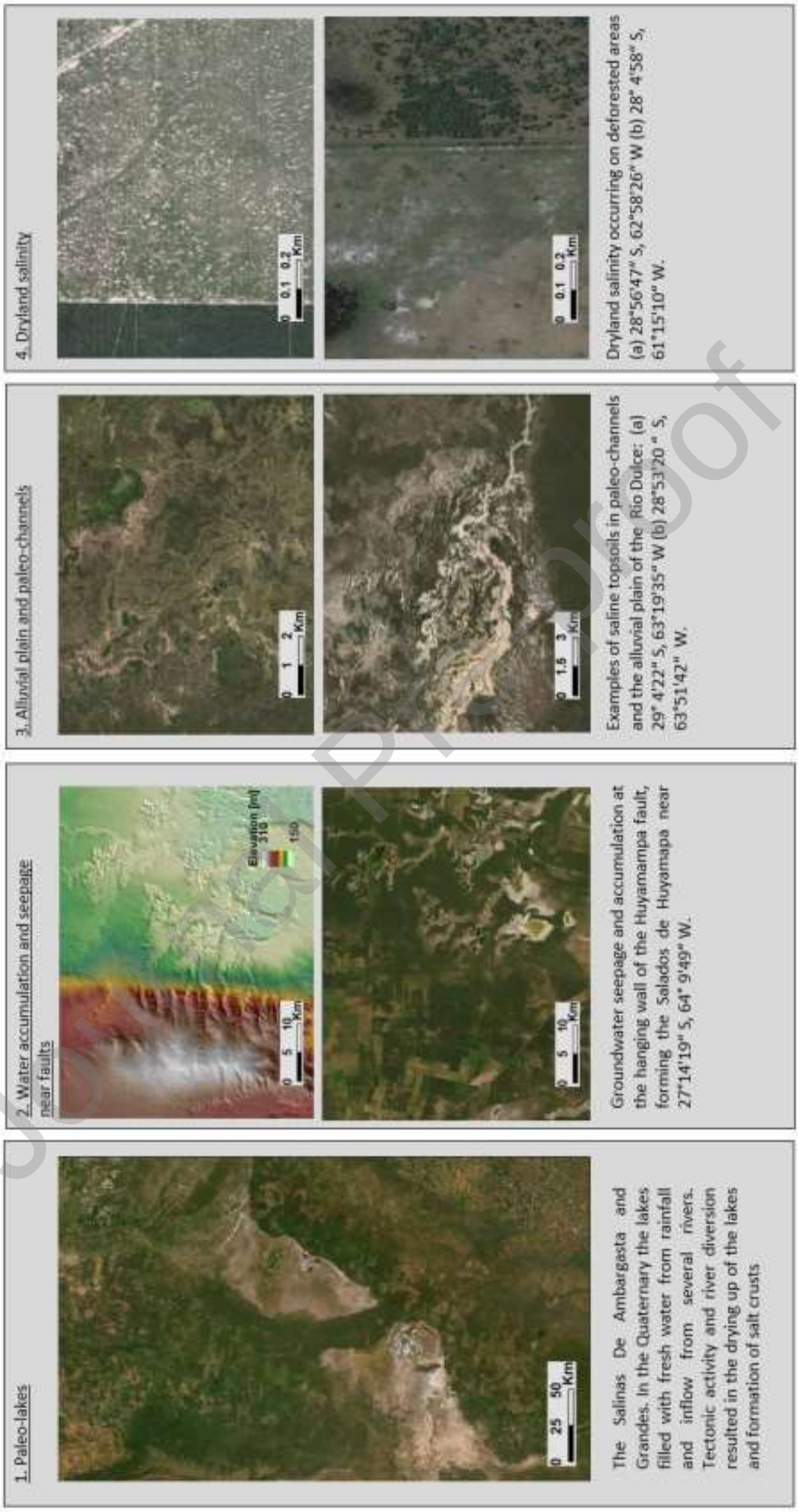

Figure A.3: Overview of different processes leading to surface soil salinity (part 1).

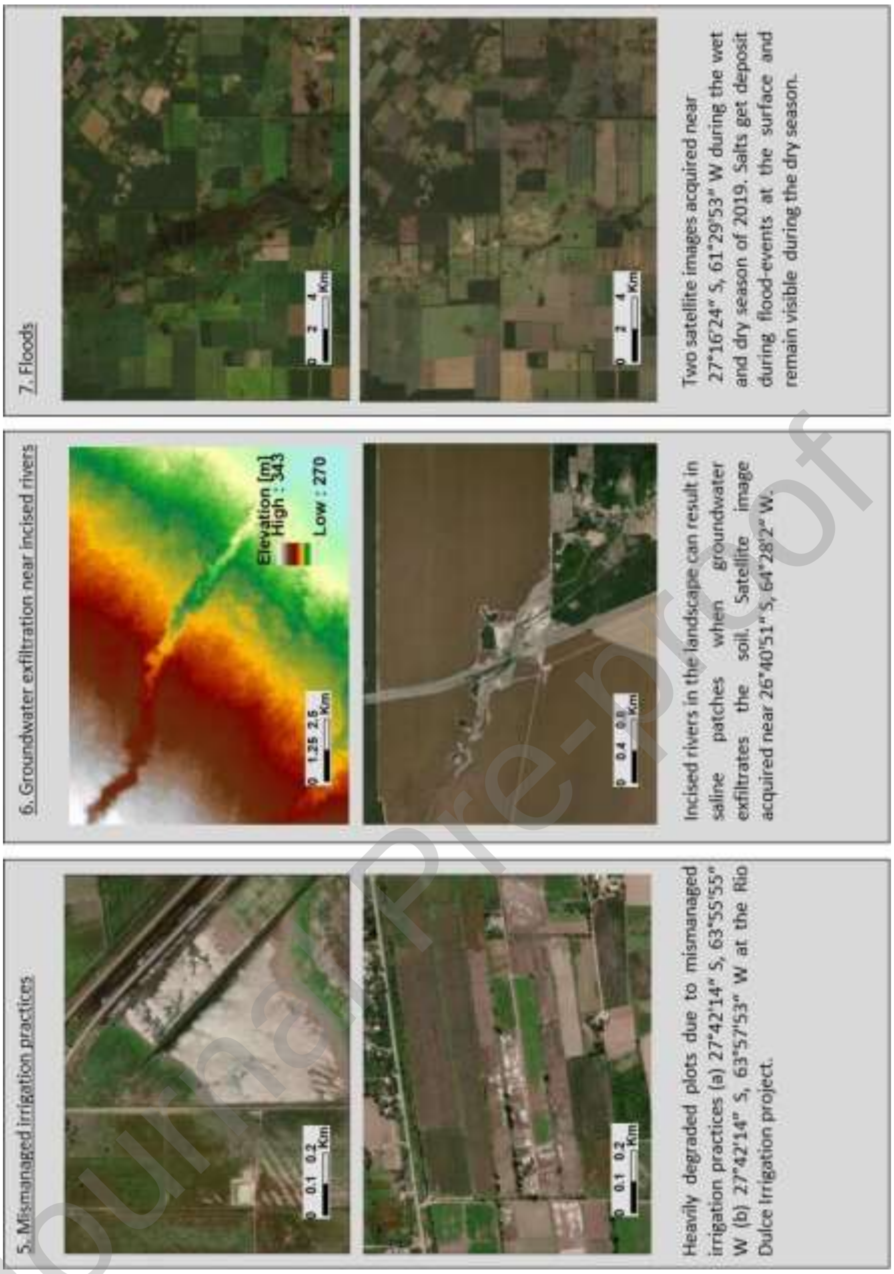

Figure A.3: Overview of different processes leading to surface soil salinity (part 2).

Declaration of interests

☒ The authors declare that they have no known competing financial interests or personal relationships that could have appeared to influence the work reported in this paper.

☐The authors declare the following financial interests/personal relationships which may be considered as potential competing interests: